MRI size assessment of cerebral microvasculature using diffusion-time-dependent stimulated-echo acquisition: A feasibility study in rodent

D.K. Lee [a], M.S. Kang [a], H. Cho [a,*]

[a] Department of Biomedical Engineering, Ulsan National Institute of Science and Technology, Ulsan, South Korea

ABSTRACT

In this study, a stimulated-echo (STE) method was employed to robustify the cerebral vessel size estimation near air-tissue, bone-tissue interfaces, and large vessels. The proposed solution is to replace the relaxation rate change from gradient-echo (GRE) with that from STE with long diffusion time after the injection of an intravascular contrast agent, superparamagnetic iron oxide nanoparticles. The corresponding diffusion length of STE is shorter than the length over which the unwanted macroscopic field inhomogeneities but is still longer than the correlation length of the fields induced by small vessels. Therefore, the unwanted field inhomogeneities are refocused, while preserving microscopic susceptibility contrast from cerebral vessels. The mean vessel diameter (dimensionless) derived from the diffusion-time-varying STE method was compared to the mean vessel diameter obtained by a conventional spin-echo (SE) and GRE combination based on Monte-Carlo proton diffusion simulations and in vivo rat experiments at 7 T. The in vivo mean vessel diameter from the MRI experiments was directly compared to available reference mouse brain vasculature obtained by a knife-edge scanning microscope (KESM), which is considered to be the gold standard. Monte-Carlo simulation revealed that SE and GRE-based MR relaxation rate changes (ΔR_2 and ΔR_2^*, respectively) can be enhanced using single STE-based MR relaxation rate change (ΔR_{STE}) by regulating diffusion time, especially for small vessels. The in vivo mean vessel diameter from the STE method demonstrated a closer agreement with that from the KESM compared to the combined SE and GRE method, especially in the olfactory bulb and cortex. This study demonstrates that STE relaxation rate changes can be used as consistent measures for assessing small cerebral microvasculature, where macroscopic field inhomogeneity is severe and signal contamination from adjacent large vessels is significant.

1. Introduction

Measurements of the changes in magnetic resonance (MR) transverse relaxation rates (from the spin-echo (SE) and gradient-echo (GRE) acquisitions) induced by the injection of an intravascular contrast agent enable the morphological quantification of the cerebral microvasculature, such as blood volume fraction (BVF), mean vessel diameter (mVD, dimensionless), and vessel size index (VSI, μm) (Boxerman et al., 1995; Dennie et al., 1998; Tropres et al., 2001). The lower bound for vessel size quantification is largely determined by the diffusion length during encoding, magnetic susceptibility difference ($\Delta\chi$) between vessels and

tissues, and magnetic field strength (B_0) (Boxerman et al., 1995; Kiselev and Posse, 1999). Under strong magnetic fields (>7 T) with the large $\Delta\chi$ values of intravascular superparamagnetic iron oxide nanoparticles (SPION), shortened echo time (TE) satisfies the static dephasing regime without losing overall sensitivity for measuring MR relaxation rates (Boxerman et al., 1995; Kiselev and Novikov, 2018). Therefore, MR sensitivity and robustness for quantifying changes in small vessel size can be enhanced. However, both increased B_0 and $\Delta\chi$ worsen the effects of macroscopic field inhomogeneity from the air- and bone-tissue interfaces and large vessel influences based on GRE acquisitions, which critically limits the robustness of conventional magnetic resonance imaging (MRI)

measurements of vessel sizes for small cerebral microvasculature (Han et al., 2015; Kim et al., 2013; Rivera-Rivera et al., 2018). Additionally, the division of relaxation rate change maps from separate GRE and SE acquisitions typically needs further adjustments from the inherently different $\Delta\chi$-dependence and the necessary co-registration of the two acquisitions. These issues are all significantly amplified under strong magnetic fields (>7 T) for small rodent brains, which limits the robust quantification of cerebral vasculatures, especially in the vicinity of the olfactory bulb (OB) and cortex.

As a result, there is a growing need to develop an optimal MR method to enhance conventional GRE acquisition to obtain regionally robust relaxation rate change for relatively small cerebral vasculatures (Han et al., 2015; Rivera-Rivera et al., 2018). Stimulated-echo (STE; $\pi/2$-TE/2-$\pi/2$-TD-$\pi/2$-TE/2) imaging method can monitor diffusive decay in the presence of inhomogeneous magnetic fields with well-defined diffusion times (TDs) for longitudinal magnetization. This method has been used to measure the pore sizes and surface-to-volume ratios of porous materials, such as trabecular bones, by measuring signal decay during TD (Song, 2000; Cho et al., 2012). However, to the best of our knowledge, no previous studies have applied the STE method to quantify the sizes of cerebral vasculature in vivo.

After the injection of intravascular contrast agent, susceptibility induced magnetic field variation exists over the length-scale of vasculatures. At long TDs for STE acquisition, water molecules diffuse sufficiently to lose significant correlations between the magnetic fields at their initial and final positions, implying that the STE signal will directly reflect the contrast of the corresponding free induction decay (FID) (Kiselev and Novikov, 2018; Song, 2000). The corresponding diffusion length is still shorter than the length over which the unwanted macroscopic fields change, therefore these unwanted fields are refocused. However, at short TDs, the contrast of STE acquisition resembles that of SE acquisition and the STE signal will produce a relaxation rate change of SE. Consequently, with dual STE acquisitions at short and long TDs for a fixed TE, separate SE- and GRE-like contrasts can be obtained without the confounding factors of GRE-induced image artifacts, such as air-tissue-interface-induced distortions and influences by adjacent larger vessels. In addition, the same STE acquisition with only different TD removes the need for image registration.

In this study, we investigated the feasibility of employing the STE imaging method to simultaneously reduce the effects of macroscopic field inhomogeneity from the air (bone)-tissue interfaces and large-vessel influences to achieve regionally robust quantification of mean vessel size for rodent brains. First, STE-derived mVD was compared to the values acquired from conventional GRE and SE methods based on Monte-Carlo (MC) proton diffusion simulations in the presence of the susceptibility-induced magnetic field inhomogeneities of randomized cylindrical objects. Second, in vivo estimation of mVD based on STE for both short (10 ms) and long (600 ms) TD acquisitions for the white matter (WM), cortex, and OB of the brain were directly compared to the results of the conventional GRE and SE methods based on a 7 T system. All results were compared to reference knife-edge scanning microscope (KESM) (Chung et al., 2011) vasculature data with a 1-μm^3 resolution, which is considered to be the gold standard for mVD measurement, to evaluate the accuracy and robustness of STE-derived in vivo mVD.

2. Methods

2.1. ΔR_2, ΔR_2^*, and ΔR_{STE} simulations

MC simulations were performed to compute changes in MR transverse relaxation-rates (ΔR_2, ΔR_2^*, and ΔR_{STE} for SE, GRE, and STE, respectively) based on previously described procedures at a B_0 of 7 T (Han et al., 2015). The finite perturber method (Pathak et al., 2008) was employed to calculate the B_0 shift of randomly distributed cylindrical models (0.4 × 0.4 × 0.4 mm^3) with various radii (each random cylinder model consisted with a single vessel radius; 2, 3, 4, 5, 6, 7, 8, 9, 10, 12, 20, and 30

μm) at blood volume fractions (BVFs; 2, 4, 6, and 8%) and a $\Delta\chi$ of 0.3 ppm (CGS unit) (Tropres et al., 2015). Identical calculations were performed at $\Delta\chi$s (0.24, 0.36, and 0.48 ppm) and a BVF of 4%. The unit grid size of the simulation was 1 μm^3, and the simulation unit time (Δt) was 1 ms. Initially, 64,000,000 (400 × 400 × 400) protons were uniformly distributed inside the simulation volume (1 proton per unit grid). The protons in the blood vessel region were removed to ignore the signal contributions of blood itself. The MC approach was employed with a periodic boundary condition at the edges of the simulation volume and without vessel permeability for proton diffusion. To be specific, with each increment of Δt, the location of each proton is changed by $N(0, 2D\Delta t)$ (independent normal random variates) with mean $\mu = 0$, and standard deviation $\sigma = \sqrt{2D \cdot \Delta t}$ from (x, y, z) to (x + N(0,2DΔt), y + N(0, 2DΔt), z + N(0,2DΔt)) (D is a diffusion coefficient equal to 1000 $\mu m^2 s^{-1}$). The phase accumulation of an nth proton during the time t, $\varphi_n(t)$, was calculated (Pathak et al., 2008):

$$\Phi_n(t) = \sum_{j=1}^{\frac{t}{\Delta t}} \gamma \Delta B(p_n(j\Delta t))\Delta t \tag{1}$$

where γ = proton gyromagnetic ratio (267.5×10^6 rad/T), $p_n(t)$ = position of nth proton at time t, $\Delta B(p)$ = magnetic field shift at position p. After the π pulse of SE and the third $\pi/2$ pulse of STE simulations, the phases of all spines were inverted to select the appropriate coherence pathways. The MR signal was determined by averaging the accumulated phase factors, which is $e^{i\phi}$, across the entire ensemble of N diffusing protons.

$$S(t) = \frac{1}{N}\sum_{n=1}^{N} e^{i\varphi_n(t)} \tag{2}$$

GRE, SE, and STE acquisitions were simulated with a TE of 10 ms. The TDs for STE were set to 10, 300, 600, 900, and 1200 ms. During the TD for STE acquisition ($\pi/2$-TE/2-$\pi/2$-TD-$\pi/2$-TE/2), the protons were diffused without phase accumulation because spins were aligned along the longitudinal direction during the TD. The phase coherence of STE acquisition (between dephasing during the first TE/2 and rephasing during the second TE/2) is modulated by adjusting the TD, which gradually loses coherence as the TD increases (Kiselev and Novikov, 2018; Song, 2000). The changes in transverse relaxation rates were calculated using the following equation:

$$\Delta R_2, \quad \Delta R_2^*, \quad and \quad \Delta R_{STE} = \frac{1}{TE}\ln\left(\frac{S_{pre}}{S_{post}}\right) \tag{3}$$

where S_{pre} (equal to one for MC simulation) and S_{post} are the signal intensity before and after administration of the contrast agent, respectively. The simulated mVD_{GRE} and VSI from the GRE and SE methods were evaluated (Tropres et al., 2015).

$$mVD_{GRE} = \frac{\Delta R_2^*}{\Delta R_2} \tag{4}$$

$$VSI = 0.424\frac{\sqrt{D}}{\sqrt{\gamma\Delta\chi B_0}}\left(\frac{\Delta R_2^*}{\Delta R_2}\right)^{\frac{3}{2}} \tag{5}$$

The corresponding mVD_{STE} from the STE method ($\Delta R_{STE, TD=300 ms\sim1200 ms}/\Delta R_{STE, TD=10 ms}$) at four different long TDs (300, 600, 900, and 1200 ms) were calculated.

$$mVD_{STE} = \frac{\Delta R_{STE, long TD}}{\Delta R_{STE, minimum TD} \text{ or } \Delta R_2} \tag{6}$$

Such mVD_{MRIs} (mVD_{GRE} and mVD_{STE}) and VSI values were obtained for various BVFs (2, 4, 6, and 8%) at fixed $\Delta\chi$ of 0.3 ppm. They were also obtained for various $\Delta\chi$s (0.24, 0.36, and 0.48 ppm) at a fixed BVF of 4% and TD of 600 ms. Then each mVD_{MRI} and VSI values were compared to

the radii of randomly distributed cylindrical models. Each calculation was repeated ten times (n = 10) with randomized cylindrical models to obtain each standard deviation.

2.2. In vivo rat experiment

Animal experiments were approved by the Institutional Animal Care and Use Committee of the Ulsan National Institute of Science and Technology. All experiments were performed under anesthesia (5% iso-flurane for induction and 2% for maintenance in 70% ambient air/30% oxygen). Body temperature was maintained by a circulating warm water tube positioned around the torso. To minimize the signal contribution from external encoding gradients during the TE, a STE sequence with a phase-cycling scheme was implemented on a Bruker 7 T scanner (Para-Vision 6.0) to select the coherence pathway of STE (Song, 2003). The ΔR_2^*p, ΔR_2, $\Delta R_{STE, \, TD=600 \, ms}$, and $\Delta R_{STE, \, TD=10 \, ms}$ values of healthy Wistar rats (n = 5) were measured using SE, STE, and multi-echo GRE acquisitions with the following parameters: pulse repetition time (TR) = 5000 ms, TE = 10 ms, number of scans = 4, acquisition resolution = $0.234 \times 0.234 \times 1 \, mm^3$, number of slices = 3 (slice gap of 5 mm to cover the cortex, WM, and OB), and contrast agent dose = 360 µmol iron/kg using SPION (injection via the tail vein). The TE for multi-echo GRE acquisition ranged from 2 to 46 ms (echo spacing of 4 ms), and the TE image of multi-echo GRE at 10 ms was used for further analysis.

SPION was synthesized according to the detailed method described by Shen et al. (1993). Briefly, a 30% solution of ammonium hydroxide was added to a solution containing dextran, ferric chloride hexahydrate, and ferrous chloride tetrahydrate, to adjust the pH to 12. The resultant colloid was then washed using hollow-fiber filtration cartridges until the iron oxide colloid was free of dextran. From this stock solution, mono-crystalline nanoparticles were recovered by ultrafiltration using hollow membrane cartridges. The characteristic of SPION used in this work is extensively documented in the previous study (Jung et al., 2014).

The core and hydrodynamic size distributions of the synthesized SPION were determined by TEM and DLS, respectively. The core size distribution of the iron oxide was 5–10 nm. The mean hydrodynamic diameter of the iron oxide nanoparticles, based on the scattering intensity distribution in a dynamic light scattering experiment, was 20±7 nm. The r_1 and r_2 of SPION were 2.36 mM^{-1}s^{-1} and 32.94 mM^{-1}s^{-1} at 7 T.

ΔR_2^*, ΔR_2, and $\Delta R_{STE, \, TD=600 \, ms}$ were calculated using Eq. (3), and the mVD$_{MRI}$s and VSI were evaluated based on Eq. Eq. (4–6). To determine the in vivo mVD$_{STE}$, $\Delta R_{STE, \, TD=10 \, ms}$ was replaced with ΔR_2 to reduce the total scan time because ΔR_2 and $\Delta R_{STE, \, TD=10 \, ms}$ provide consistent information, as discussed in the results section.

The value of experimental $\Delta \chi$ (0.255 ppm, CGS unit) was evaluated (Yablonskiy and Haacke, 1994) by measuring high-resolution (117 × 117 µm^2, slice thickness = 1 mm) steady-state ΔR_2^* values at the cortex region with 2.9% blood volume fraction (Schlageter et al., 1999) as shown in Supplementary Figure 1.

$$\Delta \chi = \frac{3 \Delta R_2^*}{4\pi \, BVF \, \gamma \, B0} \tag{7}$$

Considering the injection dose of iron (20.1 mg/kg), the previously suggested estimate of $\Delta \chi$ is 0.45 ppm (Kim et al., 2013). The value of diffusion constant was evaluated by measuring 3-direction averaged ADC values. For the direct regional comparisons with KESM results, regional apparent diffusion coefficients (ADC) for WM, cortex, and OB were respectively used as shown in Supplementary Figure 2 to minimize voxel-wise errors in VSI calculations (Tropres et al., 2015).

2.3. Mouse cerebral microvasculature

To provide a quantitative reference for MR measure of vessel sizes, three-dimensional mouse brain microvascular data was obtained from the KESM brain atlas (http://kesm.cs.tamu.edu/home/index.php). It

should be noted that only reference mouse KESM data was available. Calibrated (or normalized) comparisons were made between the rat MRI-derived vessel sizes and mouse KESM results. Because the ratio between the mean vessel radii of mouse cortex and corpus callosum regions was observed to be consistent with the corresponding ratio of rat brains (0.86 for KESM mouse brain vasculature and 0.85 for reported rat brain data (Schlageter et al., 1999)). The microvasculature was stained using an India-ink perfusion method and imaging was performed using KESM with an in-plane resolution of $0.6 \times 0.7 \, µm^2$ and a depth of 1 µm (Mayerich et al., 2008, 2011). Raw microvascular data in scalable vector graphics file format were downloaded for a slice range of 1000–7500 (corresponding to a 6.5-mm-thick volume), and the microvasculature was converted into the portable network graphics file format. The vascular region was segmented via image thresholding. Next, the microvasculature was divided into 0.5-mm-thick volumes (500 slices per volume), and each volume was resized to an isotropic resolution of $1.0 \times 1.0 \times 1.0$ µm^3. Three volumes corresponding to image slices from in vivo rat experiments were selected and voxel-wise mean vessel radius (mVR) based on KESM vasculature (mVR$_{KESM}$) was calculated using a 3D sphere-fitting method (Dougherty and Kunzelmann, 2007; Hildebrand and Rüegsegger, 1997) in the BoneJ software package (Doube et al., 2010). mVR$_{KESM}$ values less than or equal to one were excluded from further analysis because the minimum mVR$_{KESM}$ value from the 3D sphere-fitting method was one based on a unit grid size of $1.0 \times 1.0 \times 1.0$ µm^3 as shown in Supplementary Figure 3 along with three regions of interests (ROIs) of brain regions. For direct comparisons with MRI results, KESM results were averaged down to the in-plane voxel resolution of 100×100 µm^2.

2.4. Comparison of mean vessel radii between KESM and MRI

To compare KESM and MR images (using SE images before injection), three brain regions, namely the corpus callosum and associated subcortical WM, neocortex (NC), and OB, were manually segmented by referencing the Scalable Brain Atlas (Bakker et al., 2015).

Regional mVD$_{STE}$ values for each animal were first evaluated. Each regional mVD$_{STE}$ was calibrated and compared with regional mVR$_{KESM}$ values as following:

$$\text{calibrated } mVD_{STE} = \frac{\text{mean}(mVR_{KESM, \, WM})}{\text{mean}(mVD_{STE, \, WM})} \times mVD_{STE} \tag{8}$$

The rationale for the calibration of mVD$_{STE}$ is based upon the simulation results that mVR$_{KESM}$ and mVD$_{STE}$ are semi-linear in the small radius range (<5 µm). Correspondingly, both regional mVD$_{GRE}$ and VSI from GRE and SE acquisitions were evaluated and compared with regional mVR$_{KESM}$ by scatter plot of the mean.

Next to compare regional mVD$_{MRI}$ and VSI values with mVR$_{KESM}$ without vessel size variations in different animals, each in vivo mVD$_{MRI}$ was normalized with each mean (or median) mVD value in the WM and scaled relative to the mean (or median) values of mVR$_{KESM}$ in the WM.

$$\text{normalized } mVD_{MRI} = \frac{\text{mean or median}(mVR_{KESM, \, WM})}{\text{mean or median}(mVD_{MRI, \, WM})} \times mVD_{MRI} \tag{9}$$

VSI values were also accordingly normalized. Then, the normalized mVD$_{MRI}$ and VSI values for the WM, NC, and OB regions were compared with the corresponding regional mVR$_{KESM}$ employing a frequency-normalized histogram, cumulative function, and scatter plot of mean (or median) values with minimized inter-animal variations.

3. Results

3.1. MC simulation

Representative MC simulation results for randomly distributed cylindrical models are depicted in Supplementary Figure 4 and Fig. 1. The randomness of the cylinder orientation decreases as the cylinder radius
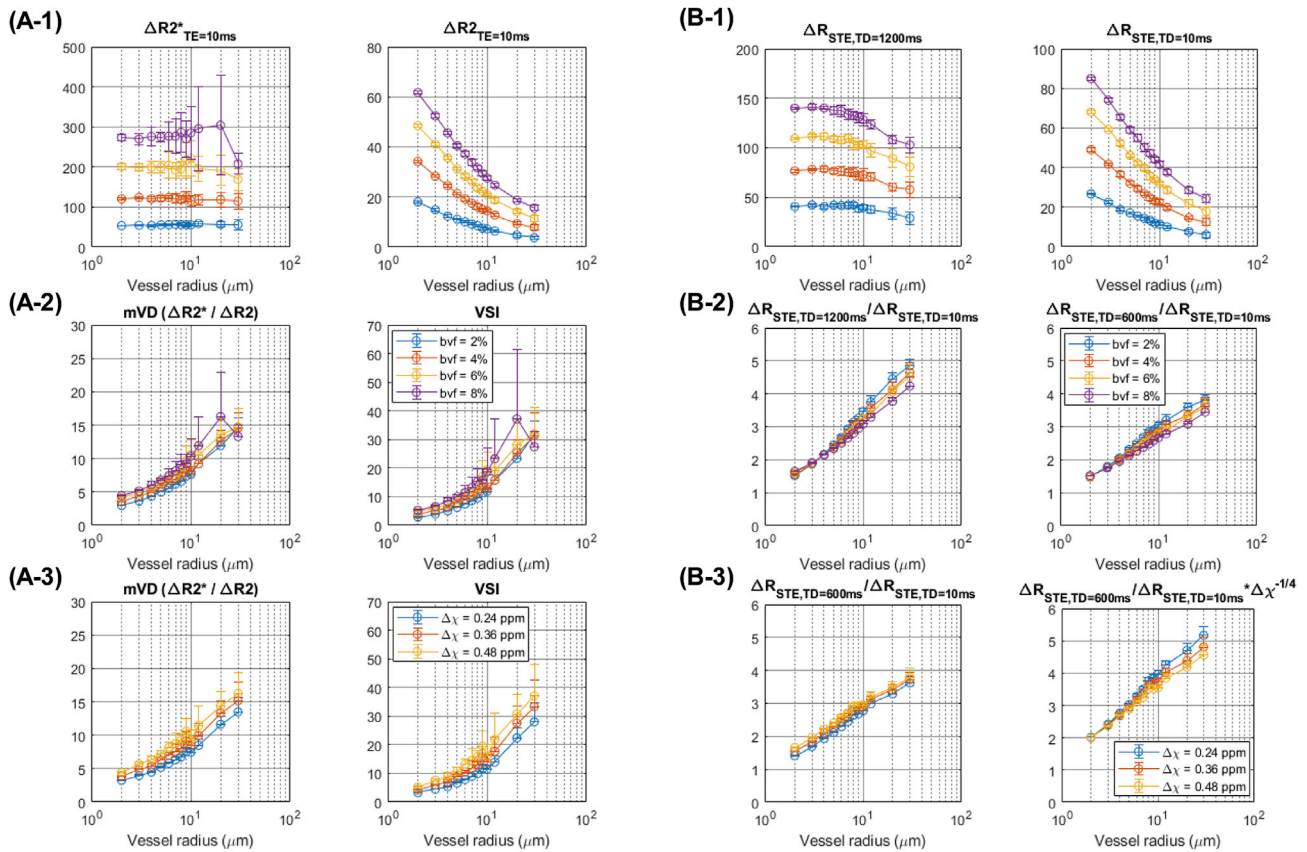
Fig. 1. Changes in MR relaxation rates (ΔR_2^*(TE = 10 ms), ΔR_2 (TE = 10 ms), and ΔR_{STE} (TE = 10 ms, TD = 10 and 1200 ms) for GRE, SE, and STE methods, respectively (A-1 and B-1) at various BVFs (2, 4, 6, and 8%) with fixed $\Delta\chi$ of 0.3 ppm (CGS unit). Conventional MRI mVD$_{GRE}$ and VSI were shown at various BVFs (2, 4, 6, and 8%) with fixed $\Delta\chi$ of 0.3 ppm (CGS unit) (A-2). Suggested mVD$_{STE}$ values of different long TD values ($\Delta R_{STE,\ TD=1200\ ms}/\Delta R_{STE,\ TD=10\ ms}$ and $\Delta R_{STE,\ TD=600\ ms}/\Delta R_{STE,\ TD=10\ ms}$) were shown at various BVFs (2, 4, 6, and 8%) with fixed $\Delta\chi$ of 0.3 ppm (CGS unit) (B-2). Conventional MRI mVD$_{GRE}$ and VSI were shown at various $\Delta\chi$ values (0.24, 0.36, and 0.48 ppm) with fixed BVF of 4% (A-3). Suggested mVD$_{STE}$ values ($\Delta R_{STE,\ TD=600\ ms}/\Delta R_{STE,\ TD=10\ ms}$ and $\Delta R_{STE,\ TD=600\ ms}/\Delta R_{STE,\ TD=10\ ms} \times \Delta\chi^{-1/4}$) were shown at fixed BVF (4%) with various $\Delta\chi$s of 0.24, 0.36, and 0.48 ppm (CGS unit) (B-3).

increases at a fixed BVF, which most likely causes the increases of standard deviation at a larger radius. For SE, GRE, STE$_{TD=10\ ms}$, and STE$_{TD=1200\ ms}$ acquisitions, the simulated phase accumulations of diffused spins whose final positions lie within each voxel ($1 \times 1 \times 400$ μm^3) after TE (and TD) evolutions were averaged ($<\varphi>$) and visualized in Supplementary Figure 4. The similarities of phase accumulations between SE versus STE$_{TD=10\ ms}$ and GRE versus STE$_{TD=1200\ ms}$ were illustrated. The phase accumulations of STE$_{TD=10\ ms}$ largely occur in the near-surface region with a randomly spread pattern, similar to those of SE. The phase accumulations of STE$_{TD=1200\ ms}$ show comparable behavior to those of GRE around the cylinder region, which is likely a result of the long diffusion length of $\sqrt{2D \cdot TD} \approx 50$ μm in the simulations. The degree of phase accumulation of the STE$_{TD=1200\ ms}$ simulation tends to decrease over a cylinder radius of approximately 10 μm as shown in Supplementary Figure 4.

Fig. 1 illustrates the computed changes in relaxation rates and corresponding mVD$_{MRI}$ and VSI values. ΔR_2^* and $\Delta R_{STE,\ TD=1200\ ms}$ are proportional to the BVF changes for small vessels and remain relatively constant compared to ΔR_2 and $\Delta R_{STE,\ TD=10\ ms}$ as the cylinder radius increases. The standard deviation of ΔR_2^* (A-1) increases as the cylinder radius and BVF increase, while that of $\Delta R_{STE,\ TD=1200\ ms}$ (B-1) appears to remain stable. $\Delta R_{STE,\ TD=1200\ ms}$ gradually decreases for large cylinder radii over 10 μm at a rate slightly higher than that of the corresponding ΔR_2^* value. ΔR_2 and $\Delta R_{STE,\ TD=10\ ms}$ exhibit an inverse relationship with the cylinder radius. $\Delta R_{STE,\ TD=10\ ms}$ is slightly larger than ΔR_2 due to the TD of 10 ms in the simulation. The computed mVD$_{GRE}$ (A-2), VSI (A-2), and mVD$_{STE}$ (B-2, $\Delta R_{STE,\ TD=600,\ 1200\ ms}/\Delta R_{STE,\ TD=10\ ms}$) values were

observed to be proportional to the cylinder radius with minimized contributions from blood volume. In particular, mVD$_{STE}$ appeared to be more or less logarithmically linear (or monotonously increasing) with respect to input vessel sizes. Specifically, for a small cylinder radius below 10 μm, mVD$_{STE}$ was observed to show smaller standard deviations compared to mVD$_{GRE}$, regardless of different BVFs. However, for cylinder radii larger than 10 μm, mVD$_{STE}$ was more consistent but appeared to underestimate vessel radii as blood volume increased. The computed mVD$_{GRE}$, VSI, and mVD$_{STE}$ values (A-3 and B-3) were also observed to be proportional to the cylinder radius at various $\Delta\chi$ values (0.24, 0.36, and 0.48 ppm) at fixed BVF (4%). Specifically, mVD$_{STE}$ values were observed to exhibit minimized contributions from $\Delta\chi$ variations. Furthermore, the adjustment of mVD$_{STE}$ values by $\sqrt[4]{\Delta\chi}$ (instead of $\sqrt[2]{\Delta\chi}$ for conventional VSI) was observed to further compensate $\Delta\chi$-dependence of TD-varying STE acquisitions up to a radius of 10 μm in estimating vessel sizes (B-3).

3.2. In vivo rat experiment

Fig. 2 depicts in vivo measurements of cerebral ΔR_2^* and $\Delta R_{STE,\ TD=600\ ms}$ values. The length of the TD (600 ms, diffusion length of $\sqrt{2D \cdot TD} \approx 34$ μm) was chosen by considering an appropriate signal-to-noise ratio (SNR) and capillary diameter of a rat brain, whose mean values are less than 5 μm (Schlageter et al., 1999). The GRE$_{pre}$ signal itself was distorted by bone-tissue and air-tissue interfaces (white arrows in the first and third row), which results in a severe underestimation of ΔR_2^* values in corresponding areas of the cortex and OB. However, no such significant signal deteriorations were observed for STE$_{pre,\ TD=600\ ms}$ in
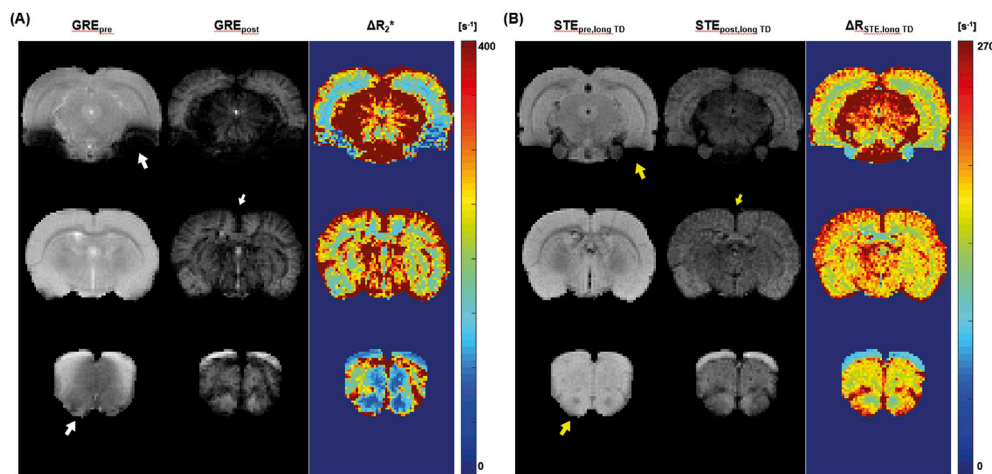
Fig. 2. In vivo changes in MR relaxation rates (ΔR_2^* and ΔR_{STE} for GRE and STE methods, respectively) for a healthy Wistar rat (208 g). ΔR_{STE} with a long TD (600 ms) (B) shows comparable results to ΔR_2^* (A) without image distortion based on macroscopic field inhomogeneity near bone-tissue and air-tissue interfaces (indicated by white arrows in (A)) and near large vessel (indicated by small white arrows in (A)). The robustness of STE acquisition near bone-tissue, air-tissue interfaces, and large vessels is indicated by yellow arrows in (B).

corresponding regions (yellow arrows in the first and third row). The GRE$_{post}$ signals are observed to decrease in a wider range near large vessels, such as sinus and pial vessels (small white arrow in the second row) than corresponding regions from the STE$_{post, \, TD=600 \, ms}$ (small yellow arrow in the second row). Corresponding ΔR_2^* values are underestimated by B_0 inhomogeneity near the bone and air interfaces. Whereas ΔR_2^* near large vessels are dominantly and likely to be overestimated by large vessels. In contrast, $\Delta R_{STE, \, TD=600 \, ms}$ is barely affected by macroscopic field inhomogeneities based on the SE-like rephasing of STE acquisition. The in vivo ΔR_2 and $\Delta R_{STE, \, TD=10 \, ms}$ values exhibit similar relaxation rates and consistent contrast, as shown in Fig. 3 and Supplementary Figure 5, and thus supports the observed TD-dependent behavior of STE acquisition from MC simulation. One can also see that $\Delta R_{STE, \, TD=10 \, ms}$ is slightly larger than ΔR_2 due to TD of 10 ms, which is consistent with the results of MC simulation.

In vivo mVD$_{GRE}$ (A), VSI (B), and mVD$_{STE}$ (C) values are mapped in Fig. 4. The in vivo results are comparable to the results of MC simulation. Specifically, one can see that mVD$_{GRE}$ and VSI values are underestimated in the areas with macroscopic field inhomogeneity based on severe bone-tissue and air-tissue interfaces, as indicated by the white arrows of the first and third rows. In contrast, mVD$_{STE}$ appears to be robust to the bone-tissue and air-tissue interface artifacts in rodent brains. The values of mVD$_{GRE}$ and VSI are larger than those of mVD$_{STE}$ in the areas around large vessels in the cortex, as shown by the white arrows in the middle row.

3.3. Reference cerebral microvasculature

A representative mouse microvasculature and the calculated mVR$_{KESM}$ values are visualized in Fig. 5. Fig. 5A presents the KESM vasculature corresponding to a single 0.5-mm-thick volume. As shown in Fig. 5B and C, BVF and mVR$_{KESM}$ exhibit a clear difference between the NC and WM regions. Both the mVR$_{KESM}$ and BVF values of the NC region with penetrating vessels are larger than those of the WM region.

3.4. Comparison between mVR$_{KESM}$ and mVD$_{MRI}$

Fig. 6A presents scatter-plot comparisons (regional mean values) of mVD$_{STE}$ (A-1), calibrated mVD$_{STE}$ (A-2), mVD$_{GRE}$ (A-3), and VSI (A-4) values (n = 5) with respect to mVR$_{KESM}$. The regional values of mVD$_{STE}$ were smaller than those of mVR$_{KESM}$, and consistently followed the marked blue line ($y = \frac{mean(mVD_{STE, \, WM})}{mean(mVR_{KESM, \, WM})} x$). Then, calibrated mVD$_{STE}$ (with a calibration factor of 1.38) was in agreement (r = 0.69, p < 0.005) with respect to mVR$_{KESM}$. The values of mVD$_{GRE}$ and VSI showed reduced linearity (r = 0.57 and 0.56, p < 0.05) with respect to mVR$_{KESM}$, and under- and overestimations of vessel sizes in OB and cortex regions were respectively observed.

To further remove potential vessel size variations among each animal, each regional mean value of mVD$_{STE}$ (B-1), mVD$_{GRE}$ (B-2), and VSI (B-3) was normalized with respect to the corresponding mean mVR$_{KESM}$ value
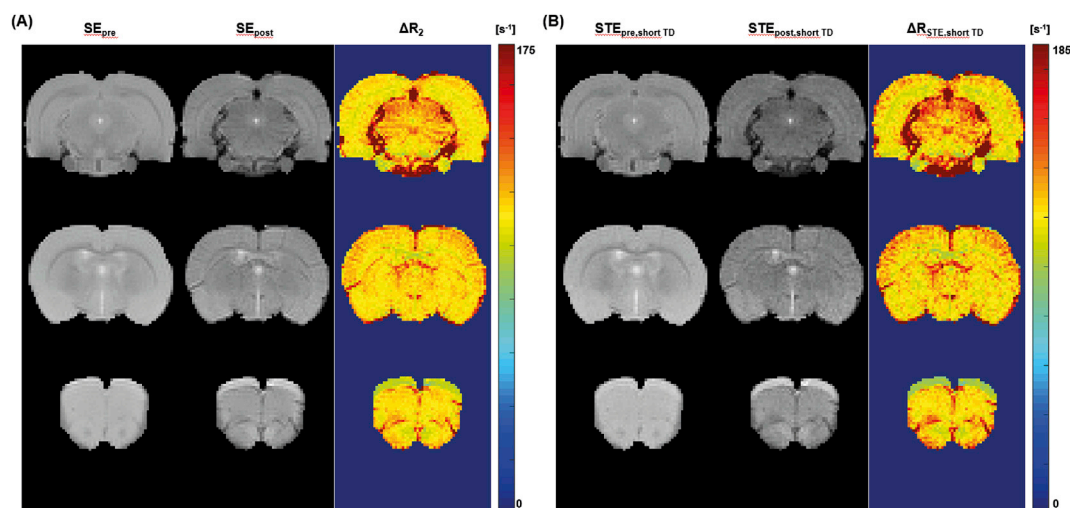

Fig. 3. In vivo changes in MR relaxation rates (ΔR_2 and ΔR_{STE} for SE and STE methods, respectively) for a healthy Wistar rat (208 g). ΔR_{STE} with a short TD (10 ms) (B) shows comparable results to ΔR_2 (A).
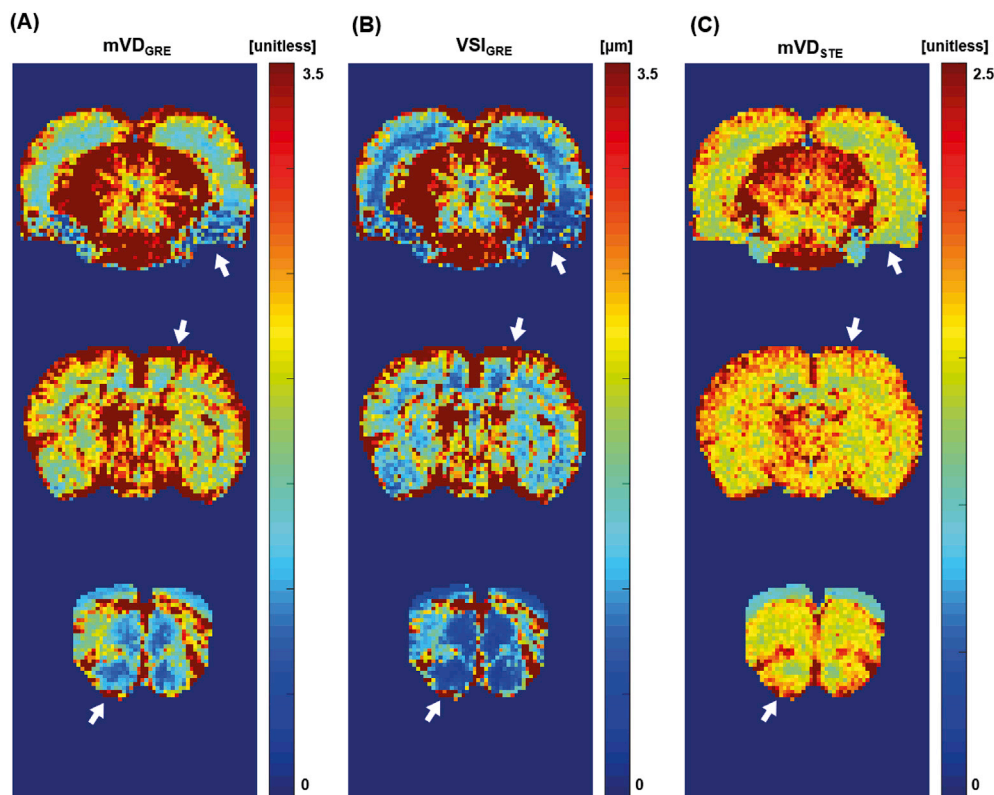
Fig. 4. In vivo results of GRE- and SE-based MRI mVD_{GRE} ($\Delta R_2^*/\Delta R_2$, unitless) (A) and VSI_{GRE} (μm) (B) and STE-based mVD_{STE} ($\Delta R_{STE,\,longTD}/\Delta R_2$, unitless) (C) for a Wistar rat (208 g). The mVD of the STE method (C) shows comparable results to mVD and VSI of the GRE and SE combined method (A and B) without image distortions caused by macroscopic field inhomogeneity from the bone (or air)- tissue interfaces and large vessel influences near skulls (white arrows). The value of experimental $\Delta\chi$ (0.255 ppm, CGS unit) was evaluated by measuring high-resolution (117 × 117 μm², thickness = 1 mm) steady-state ΔR_2^* values at the cortex region ($\Delta\chi = \frac{3}{4\pi}\frac{\Delta R_2^*}{BVF\,\gamma\,B0}$) with a 2.9% blood volume fraction. The value of diffusion constant was evaluated by measuring 3-direction averaged ADC values.
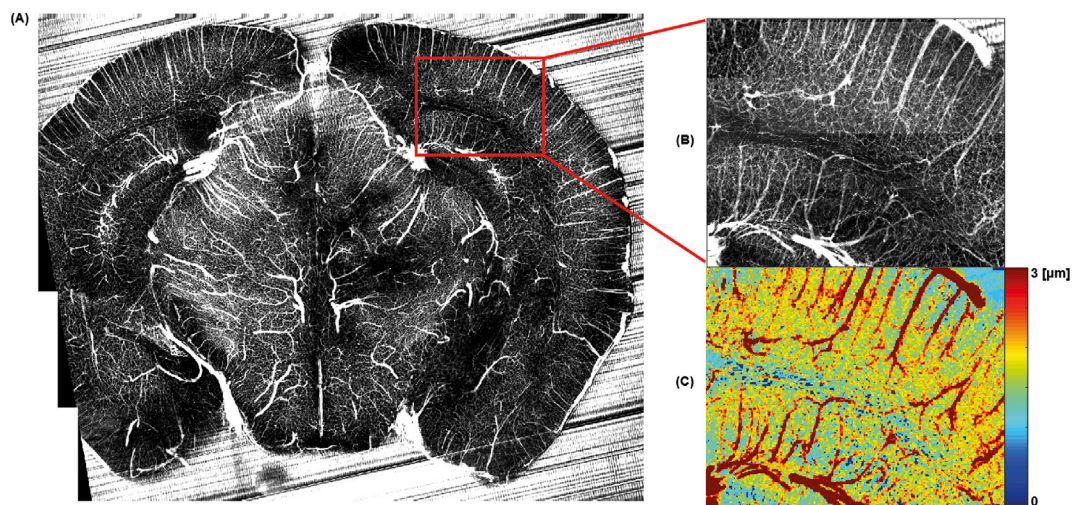

Fig. 5. Three-dimensional mouse brain microvascular data from the KESM Brain Atlas (A). BVF of the cortex and WM regions, and corresponding mVR_{KESM} map calculated using a sphere-fitting method (B and C).

of WM region as described in the method section 2.4. Improved linearity ($r = 0.85$, $p < 0.001$) of normalized mVD_{STE} with respect to mVR_{KESM} was observed in comparison with normalized mVD_{GRE} ($r = 0.65$, $p < 0.01$) and normalized VSI ($r = 0.63$, $p < 0.05$). Under- and overestimations of vessel sizes in OB and cortex regions were still conspicuous for the GRE-based method.

Fig. 7 presents comparison results between distributions of mVR_{KESM} values and normalized (with respect to the median value of mVR_{KESM} in WM region) mVD_{MRI} (mVD_{STE} and mVD_{GRE}) values. ROIs for MRI and KESM vasculature are highlighted in Fig. 7A and Supplementary Figure 3, respectively. KESM results were averaged down to the voxel resolution of 100 × 100 μm² for direct comparisons with MRI results.

Frequency-normalized histograms of mVR_{KESM}, normalized mVD_{STE}, and normalized mVD_{GRE} are compared in Figs. 7B–1 (WM), 7B-2 (NC), and 7B-3 (OB). For mVR_{KESM} and normalized mVD_{STE}, the median of each ROI is similar, and the median of the WM region is smaller than those of the NC and OB regions (WM < OB < NC). In contrast, normalized mVD_{GRE} in the OB region exhibits an underestimated median value based on macroscopic field inhomogeneity caused by air-tissue interfaces. Compared to mVR_{KESM}, the median of normalized mVD_{GRE} in the NC region is relatively overestimated based on the presence of large penetrating vessels (OB < WM < NC), as shown in Fig. 2A. The cumulative functions show consistent results as shown in Figs. 7C–1 (WM), 7C-2 (NC), and 7C-3 (OB). For normalized mVD_{GRE}, an intersection in the
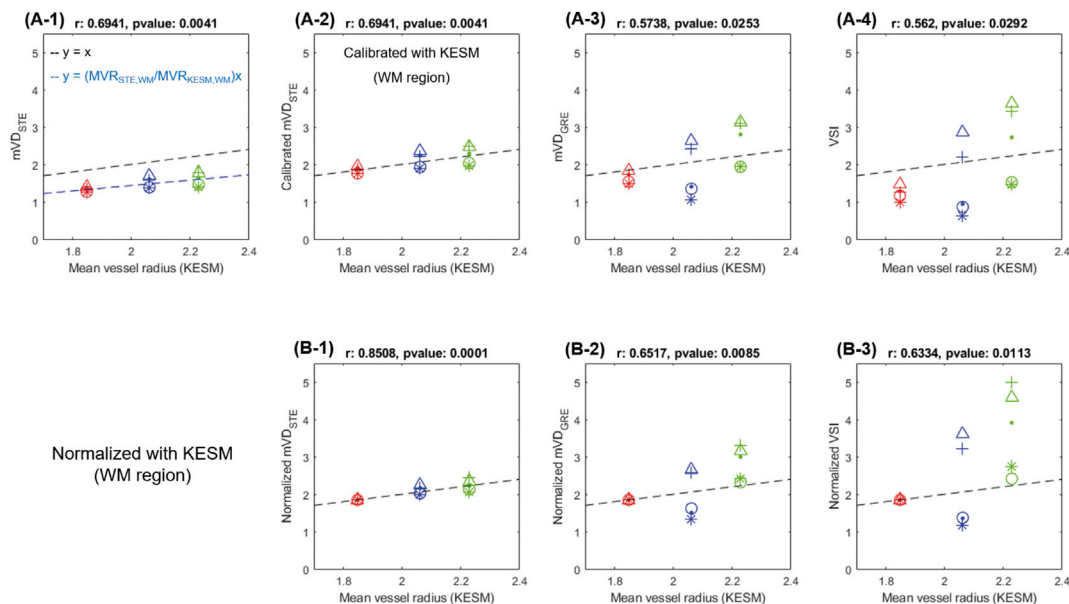
Fig. 6. Regional comparisons (red: WM, blue: OB, and green: NC) between mVR_{KESM} with mVD_{STE} (A-1), calibrated mVD_{STE} (A-2), mVD_{GRE} (A-3), and VSI (A-4). Mean normalized mVD_{STE} (B-1), mVD_{GRE} (B-2), and VSI (B-3) are also shown to reduce vessel size variations among animals from the direct regional comparison with mVR_{KESM}.
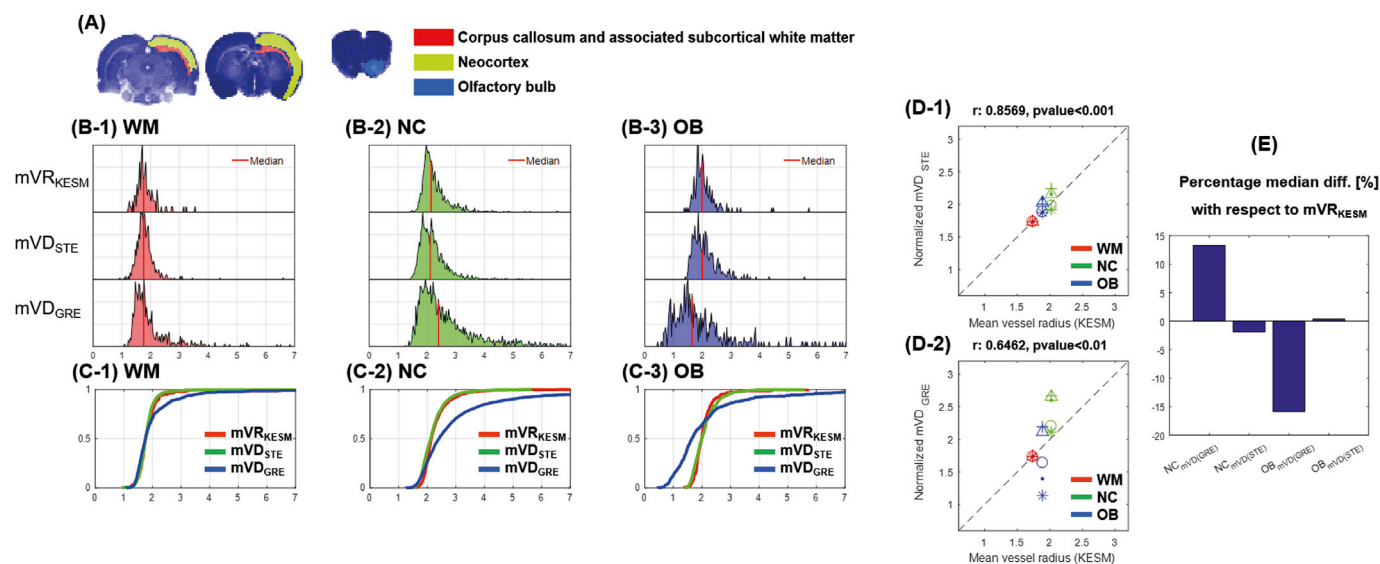

Fig. 7. Regional comparisons between mVR_{KESM} and in vivo mVD_{MRI}s (mVD_{GRE} and mVD_{STE} from $\Delta R_2^*/\Delta R_2$ and $\Delta R_{STE, TD=600 ms}/\Delta R_2$, respectively). MRI results from rat brains (n = 5) were combined for the analysis. KESM results were averaged down to the in-plane voxel resolution of $100 \times 100\ \mu m^2$ for direct comparisons with MRI results. Three ROIs from pre-injection SE images (A). Frequency-normalized histograms of mVR_{KESM}, median normalized mVD_{STE}, and median normalized mVD_{GRE} values for WM (B-1), NC (B-2), and OB (B-3). Cumulative functions of mVR_{KESM} and median normalized mVD_{STE}, and median normalized mVD_{GRE} values for WM (C-1), NC (C-2), and OB (C-3). By referencing the mVR_{KESM}, the scatter plots of median normalized mVD_{STE} (D-1) and median normalized mVD_{GRE} (D-2) were compared for the three ROIs. Percentage differences (%) between median values of mVD_{MRI}s for five normal rat brains (n = 5) and reference KESM values were shown for each region (E).

cumulative function occurs at a small radius due to the underestimation in the OB region. Saturation of the cumulative function of normalized mVD_{GRE} in the NC region is particularly slower than that of mVR_{KESM} due to the overestimation in the corresponding region. The cumulative function of normalized mVD_{STE} closely matches that of mVR_{KESM} in all regions, while the normalized mVD_{STE} appears to lose some of the large vessel information, which is likely caused by the decreasing $\Delta R_{STE, longTD}$ values of large vessel radii based on the limited length of the TD, as shown in the corresponding MC simulations. The vessel size overestimation in the NC and underestimation in the OB of the normalized mVD_{GRE} are conspicuous, but the size estimations based on normalized

mVD_{STE} are consistent with respect to mVR_{KESM} in the scatter plot of median values (n = 5), as shown in Figs. 7D–1 and 7D-2. Percentage differences (%) of median mVD_{MRI}s ((mVD_{MRI}s − mVR_{KESM})/mVR_{KESM} × 100) in the region of NC and OB for GRE and STE acquisitions were plotted in Fig. 7E. Vessel size underestimation for OB and overestimation for NC from GRE acquisition was apparent, while corresponding errors were within 3% from STE acquisition.

4. Conclusions and discussion

As a method for overcoming the limitations of conventional GRE and

SE combined acquisitions for MR measurement of vessel size, the feasibility of the proposed diffusion-time regulated STE method was demonstrated through MC simulations and in vivo rat experiments using a 7 T system, focused on accurately quantifying and distinguishing small microvessels. The MC simulations revealed that changes in MR relaxation rates based on STE acquisition (ΔR_{STE}) provide the vessel size information by regulating the length of the TD. The microvessel-related information of ΔR_{STE} between long and short TDs was comparable to that of the GRE and SE methods, respectively. The simulated ΔR_{STE} value with a long TD tended to decrease at a large cylinder radius (radius > 10 μm), which supports the in vivo observations that macroscopic field inhomogeneities from large vessels, air-tissue, and bone-tissue interfaces are reduced by the STE method. Experimentally, from the direct comparisons with respect to the KESM method using India-Ink blood vessel staining, both vessel size underestimation caused by macroscopic field inhomogeneity in the OB region and the influences of large vessels (penetrating vessels and pial cortical veins) in the NC region of GRE-based relaxation rate were observed to be significantly reduced in the STE-based relaxation rate with a long TD. However, it should be noted that this poses a limitation for STE acquisition in terms of underestimating larger cerebral vasculature. Correspondingly, the in vivo mVD_{STE} value of $\Delta R_{STE,\ longTD}/\Delta R_2$ was successfully obtained and observed to be robust compared to the conventional mVD_{GRE} and VSI values in WM, OB, and cortical regions of rodent brains. These results were corroborated by the corresponding gold-standard mVR_{KESM} results. Although, all experiments were conducted in rats, in vivo mean vessel diameter from the MRI experiments was directly compared to reference mouse brain vasculature obtained by a KESM (Mayerich et al., 2011). Although we are aware of inter-species differences in the cerebrovascular (Kim et al., 2017; Boswell et al., 2014), this was done because of the lack of availability of high-resolution rat microvasculature data in the public domain. Moreover, we found that the ratio between the vessel radii of mouse cortex and corpus callosum regions was observed to be similar to that reported for rat brains (0.86 for KESM mouse brain vasculature and 0.85 for reported rat brain data (Schlageter et al., 1999)).

It should be noted that absolute vessel size quantification from STE acquisition is still required with rigorous analytical approaches. Various MC simulation with varying BVFs, vessel radii, TDs, and $\Delta\chi$ values in this study provided insights into the asymptotic behavior of TD-dependent behavior of STE acquisition for vessel size estimation. However, due to potential discrepancies in the simulation approach, analytical formulas are used for absolute quantification of conventional vessel size imaging, which also corresponds to STE acquisition. In this study, we specifically aimed to demonstrate the feasibility and benefits of STE acquisition for quantifying small vessels in OB and cortex areas, where conventional methods are known to deteriorate. As a result, the experimental mVD_{STE} values were linearly calibrated (or normalized) with respect to the corresponding KESM results in the white matter region, without rushing to absolute quantification based on the asymptotic simulation results in this study with a limited range of experimental vessel sizes. In order to investigate the feasibility of absolute quantification of vessel size with TD-dependent STE acquisition, it is necessary to explore rigorous analytical derivation at different encoding regimes of STE acquisition to determine the functional dependence of mVD_{STE} on actual vessel sizes. And such functional form should be experimentally verified across different species of a wider range of vessel sizes. This is considered to be beyond the scope of the current feasibility study and we hope that these measurements challenge the theory for more robust vessel size imaging.

There are potential adjustments for improvements related to the STE method for measuring mean vessel size. First, the signal strength of STE acquisition is half that of SE acquisition and T_1 relaxation during the TD (proportional to $e^{-TD/T1}$) reduces the SNR as the TD becomes longer. However, to obtain purely FID-like contrast from STE acquisition, the diffusion length (34 μm for TD = 600 ms in our experiment) during the TD should be sufficiently larger than the length of coherent susceptibility field variations due to cerebral vasculature of subject brains. Therefore,

tradeoffs between SNR and ΔR_2^* contrast from varying TDs should be considered for potential clinical applications with larger vessel sizes (Duvernoy et al., 1983; Lauwers et al., 2008). Supplementary Figure 6 shows TD (300, 600, 900, and 1200 ms) dependent behavior of vessel size estimation for this purpose. Considering the fact that the human capillary radius in the cerebral cortex is 3.23 ± 0.85 μm (Duvernoy et al., 1983), the minimum TD value over 600 ms appears to be necessary from simulation results for clinical applications. More theoretical studies will highlight the applicability of STE-based vessel size estimation to various vessel sizes and inter-vessel distances. Second, to cover the entire imaging region, the TR for STE_{longTD} should be lengthened based on the TD and multi-slice acquisition, which increases the total scan time and sensitivity to motion artifacts because the signal encoding duration of the STE method (TE + TD) is longer than that of GRE acquisition (TE). Limitations based on the SNR and elongated scan time of STE acquisition can be resolved by using multiple array coils and acquisition acceleration techniques, such as compressed sensing and parallel acquisition (Lustig et al., 2007). Third, the possibility of obtaining vessel size distribution information from a single image voxel remains to explored with TD varying STE acquisitions. With well-regulated diffusion length from TD at fixed TE, the Laplace inversion of STE signal decay as a function of TD can potentially provide vessel size distribution from a single image voxel.

In conclusion, TD-dependent STE-based MR relaxation rates ($\Delta R_{STE,\ longTD}$ and $\Delta R_{STE,\ shortTD}$) provide a robust measure for assessing the size of small cerebral microvasculature without co-registering GRE and SE acquisitions, especially where macroscopic field inhomogeneity and large vessel contaminations are significant.

CRediT authorship contribution statement

D.K. Lee: Writing - original draft, Investigation. **M.S. Kang:** Writing - original draft, Validation. **H. Cho:** Writing - original draft, Conceptualization, Supervision, Investigation.

Appendix A. Supplementary data

Supplementary data to this article can be found online at https://doi.org/10.1016/j.neuroimage.2020.116784.

References

Bakker, R., Tiesinga, P., Kotter, R., 2015. The scalable brain atlas: instant web-based access to public brain atlases and related content. Neuroinformatics 13, 353–366.

Boswell, C.A., Mundo, E.E., Ulufatu, S., Bumbaca, D., Cahaya, H.S., Majidy, N., Van Hoy, M., Schweiger, M.G., Fielder, P.J., Prabhu, S., Khawli, L.A., 2014. Comparative physiology of mice and rats: radiometric measurement of vascular parameters in rodent tissues. Mol. Pharm. 11 (5), 1591–1598.

Boxerman, J.L., Hamberg, L.M., Rosen, B.R., Weisskoff, R.M., 1995. MR contrast due to intravascular magnetic-susceptibility perturbations. Magn. Reson. Med. 34, 555–566.

Cho, H.J., Sigmund, E.E., Song, Y.Q., 2012. Magnetic resonance characterization of porous media using diffusion through internal magnetic fields. Materials 5, 590–616.

Chung, J.R., Sung, C., Mayerich, D., Kwon, J., Miller, D.E., Huffman, T., Abbott, L.C., Keyser, J., Choe, Y., 2011. Multiscale exploration of mouse brain microstructures using the knife-edge scanning microscope brain atlas. Front. Neuroinf. 5, 29.

Dennie, J., Mandeville, J.B., Boxerman, J.L., Packard, S.D., Rosen, B.R., Weisskoff, R.M., 1998. NMR imaging of changes in vascular morphology due to tumor angiogenesis. Magn. Reson. Med. 40, 793–799.

Doube, M., Klosowski, M.M., Arganda-Carreras, I., Cordelieres, F.P., Dougherty, R.P., Jackson, J.S., Schmid, B., Hutchinson, J.R., Shefelbine, S.J., 2010. BoneJ: free and extensible bone image analysis in ImageJ. Bone 47, 1076–1079.

Dougherty, R., Kunzelmann, K.-H., 2007. Computing local thickness of 3D structures with ImageJ. Microsc. Microanal. 13, 1678–1679.

Duvernoy, H., Delon, S., Vannson, J., 1983. The vascularization of the human cerebellar cortex. Brain Res. Bull. 11, 419–480.

Han, S.H., Cho, J.H., Jung, H.S., Suh, J.Y., Kim, J.K., Kim, Y.R., Cho, G., Cho, H., 2015. Robust MR assessment of cerebral blood volume and mean vessel size using SPION-enhanced ultrashort echo acquisition. Neuroimage 112, 382–389.

Hildebrand, T., Rüegsegger, P., 1997. A new method for the model-independent assessment of thickness in three-dimensional images. J. Microsc. 185, 67–75.

Jung, H., Park, B., Lee, C., Cho, J., Suh, J., Park, J., Kim, Y., Kim, J., Cho, G., Cho, H., 2014. Dual MRI T1 and T2 (*) contrast with size-controlled iron oxide nanoparticles. Nanomed. Nanotechnol. Biol. Med. 10 (8), 1679–1689.

Kim, S.G., Harel, N., Jin, T., Kim, T., Lee, P., Zhao, F., 2013. Cerebral blood volume MRI with intravascular superparamagnetic iron oxide nanoparticles. NMR Biomed. 26, 949–962.

Kim, M.J., Kim, Y.Y., Chao, J.R., Park, H.S., Chang, J., Oh, D., Lee, J.J., Kang, T.C., Suh, J.G., Lee, J.H., 2017. Comparing the organs and vasculature of the head and neck in five murine species. in vivo, 31 (5), 861–871.

Kiselev, Valerij G., Novikov, Dmitry S., 2018. Transverse NMR relaxation in biological tissues. Neuroimage 182, 149–168.

Kiselev, V.G., Posse, S., 1999. Analytical model of susceptibility-induced MR signal dephasing: effect of diffusion in a microvascular network. Magn. Reson. Med. 41, 499–509.

Lauwers, F., Cassot, F., Lauwers-Cances, V., Puwanarajah, P., Duvernoy, H., 2008. Morphometry of the human cerebral cortex microcirculation: general characteristics and space-related profiles. Neuroimage 39, 936–948.

Lustig, M., Donoho, D., Pauly, J.M., 2007. Sparse MRI: the application of compressed sensing for rapid MR imaging. Magn. Reson. Med. 58, 1182–1195.

Mayerich, D., Abbott, L., McCormick, B., 2008. Knife-edge scanning microscopy for imaging and reconstruction of three-dimensional anatomical structures of the mouse brain. J. Microsc. 231, 134–143.

Mayerich, D., Kwon, J., Sung, C., Abbott, L., Keyser, J., Choe, Y., 2011. Fast macro-scale transmission imaging of microvascular networks using KESM. Biomed. Optic Express 2, 2888–2896.

Pathak, A.P., Ward, B.D., Schmainda, K.M., 2008. A novel technique for modeling susceptibility-based contrast mechanisms for arbitrary microvascular geometries: the finite perturber method. Neuroimage 40, 1130–1143.

Rivera-Rivera, L.A., Schubert, T., Knobloch, G., Turski, P.A., Wieben, O., Reeder, S.B., Johnson, K.M., 2018. Comparison of ferumoxytol-based cerebral blood volume estimates using quantitative R1 and relaxometry. Magn. Reson. Med. 79, 3072–3081.

Schlageter, K.E., Molnar, P., Lapin, G.D., Groothuis, D.R., 1999. Microvessel organization and structure in experimental brain tumors: microvessel populations with distinctive structural and functional properties. Microvasc. Res. 58, 312–328.

Shen, T., Weissleder, R., Papisov, M., Bogdanov Jr., A., Brady, T.J., 1993. Monocrystalline iron oxide nanocompounds (MION): physicochemical properties. Magn. Reson. Med. 29 (5), 599–604.

Song, Y.-Q., 2000. Determining pore sizes using an internal magnetic field. J. Magn. Reson. 143, 397–401.

Song, Y.Q., 2003. Using internal magnetic fields to obtain pore size distributions of porous media. Concepts Magn. Reson. Part A: An Educational Journal 18, 97–110.

Tropres, I., Grimault, S., Vaeth, A., Grillon, E., Julien, C., Payen, J.F., Lamalle, L., Decorps, M., 2001. Vessel size imaging. Magn. Reson. Med. 45, 397–408.

Tropres, I., Pannetier, N., Grand, S., Lemasson, B., Moisan, A., Peoc'h, M., Remy, C., Barbier, E.L., 2015. Imaging the microvessel caliber and density: principles and applications of microvascular MRI. Magn. Reson. Med. 73, 325–341.

Yablonskiy, D.A., Haacke, E.M., 1994. Theory of NMR signal behavior in magnetically inhomogeneous tissues: the static dephasing regime. Magn. Reson. Med. 32 (6), 749–763.